ORIGINAL RESEARCH ARTICLE

Precipitate Structure, Microstructure Evolution Modeling and Characterization in an Aluminum Alloy 7050 Friction Stir Weld

Ralph Bush, Ioan Feier, and David Diercks

Novel use of differential scanning calorimetry (DSC), with 1.7 mm specimen spacing intervals across a friction stir weld, coupled with microhardness, electrical conductivity, transmission electron microscopy (TEM), and novel three-dimensional thermal modeling of temperature profiles were used to characterize precipitate structure as a function of position across a friction stir welded and post-weld stabilized aluminum alloy 7050. The results show excellent agreement with predictions of existing FSW microstructural evolution models for 7XXX aluminum alloys. The DSC scans and thermal modeling accurately predicted the locations and peak temperatures at which transitions from 1) slow precipitate dissolution to 2) rapid dissolution, coarsening, and transformation of η' to η precipitates to 3) increasing η dissolution and matrix supersaturation occur along the weld. These results are correlated to significant changes in the microhardness and electrical conductivity profiles. Following a 12-year period after the initial post-weld stabilization treatment, the closely spaced DSC scans were able to show that the initial stabilization treatment, (a standard T6 heat treatment), had not fully stabilized the weld near the heat affected zone (HAZ) hardness minimum. A 2-step stabilization method is proposed to fully stabilize the material in this region of the weld.

List of Symbols	
ρ	Density, kg/m^3
C_p	Specific heat, J/(kg·C)
k	Thermal conductivity, W/(m·C)
S	Volumetric heat generation, W/m^3
T	Temperature, C
u	Tool translation speed (m/s or mm/s)
x, y, z	Coordinates for spatial location, (m or mm)
HV	Vickers hardness
η'	Metastable precipitate phase intermediate to GP zones and η phase
η	Final stable precipitate phase

1. Introduction

Friction stir welding is a solid-state welding process that is particularly useful for the joining of highly alloyed aluminum alloys in the 2XXX and 7XXX families. These alloys are normally considered unweldable by conventional fusion welding techniques due to the tendency to crack during cooling (Ref 1). Significant cost savings in fabrication of structures via elimination of fasteners could be realized by welding these materials instead of the standard methods of riveting and bolting used currently.

Short duration high temperature exposures of a non-isothermal nature and plastic deformation are experienced by the material during friction stir welding. The different temperature exposures and deformation paths experienced at different locations within the weld have a significant effect on the size, volume fraction, type, and behavior of strengthening precipitates in the material. Previous studies show that precipitate

dissolution, coarsening, and re-precipitation occur to varying degrees at different locations within a weld (Ref 2-7). The extent to which each of these precipitate behaviors occur is primarily a function of the maximum temperature experienced, the time at which the material spends at elevated temperatures during welding and the precipitate stability, which in turn are functions of the welding parameters utilized, alloy chemistry, and the initial temper of the material (Ref 2, 3, 8-16). The ability to easily measure and model the precipitate evolution during FSW and to correlate the structure with the mechanical properties and corrosion response of these welds is critical for optimization of welding parameters and design of structural parts.

Microhardness profiles of friction stir welds are commonly used as a measure of weld structure. The profiles can also be used as a rough indicator of the macroscopic weld zone

Ralph Bush and **Ioan Feier**, Department of Mechanical Engineering, US Air Force Academy, Colorado Springs, CO; and **David Diercks**, Department of Metallurgical and Materials Engineering, Colorado School of Mines, Golden, CO. Contact e-mails: bushrbw@gmail.com and bushbrr@gmail.com.

locations and precipitate structure. The microhardness profile of precipitation strengthened 7XXX aluminum alloys that are friction stir welded in either the T6 or T7X temper typically exhibits a W-shape when the peak temperature approaches or exceeds the precipitate solvus temperature. (Ref 2, 7, 10, 16, 17) The weld nugget (WN) encompasses the volume through which the pin traverses plus a small volume on either side. The temperatures in the WN approach or exceed the solvus temperature ($\sim$ 427 C) resulting in complete dissolution of the original precipitates. A small number of stable precipitates are often noted to heterogeneously nucleate at grain boundaries, dispersoids, or constituent particles during cooling. Immediately after welding, the precipitate microstructure consists only of these few large precipitates. Guinier–Preston zones (GP zones) will form if the material is allowed to naturally age at room temperature with the volume fraction and size increasing over several years. This is accompanied by a concomitant increase in hardness (Ref 18-21). If a stabilizing post-weld aging treatment is applied, the precipitate microstructure and hardness of the WN approaches that associated with the post-weld aging temperature and time (Ref 3, 5, 10, 18). The thermo-mechanical affected zone (TMAZ) consists of the WN plus unrecrystallized surrounding material that has been deformed by the stirring weld pin. The material hardness in the unrecrystallized volume decreases monotonically with increasing distance from the weld center to the hardness minimum. The outer extent of the TMAZ is often located near the hardness minimum. Precipitate microstructure in the TMAZ of 7XXX aluminum alloys consists of a low volume fraction of very coarse η precipitates in a matrix that is supersaturated at room temperature (Ref 2-5, 7). Maximum temperatures reached in the TMAZ during welding typically range between 320 and 350 C, at the hardness minimum, and 400-450 C near the WN (Ref 7, 8, 10, 16). Precipitate response to a post-weld aging treatment is a combination of coarsening and formation of new, smaller GP zones or η' precipitates. Near the WN this usually results in a small increase in hardness, whereas near the hardness minimum a decrease in hardness is generally observed as there is insufficient supersaturation of solute for a sufficient quantity of new precipitation to override the softening caused by coarsening. The heat affected zone (HAZ) is characterized as the material in which no plastic deformation has occurred during welding, but the thermal transient imposed is sufficient to cause precipitate coarsening and/or dissolution. Precipitate response to a rapidly applied, short lived thermal transient is rapid dissolution to a volume fraction below the equilibrium level, followed by an increase in volume fraction to equilibrium levels and coarsening. The amount and rate of dissolution and coarsening increase with temperature. At lower temperatures and the short times experienced in FSW there is insufficient time to reach the coarsening stage. At higher temperatures there is sufficient time for both the dissolution and coarsening stages (Ref 2, 3, 6-25). For typical FSW thermal histories, dissolution unaccompanied by significant coarsening occurs when the maximum temperature remains below about 220-250 C (Ref 3). Coarsening is of greater consequence in areas where the maximum temperature reaches 250 C or greater. Hardness in the HAZ increases monotonically as distance from the weld center increases. There is little to no response to a post-weld age in the region of the HAZ farthest from the weld center due to insufficient matrix supersaturation to nucleate new precipitates. The region of the HAZ closest to the hardness minimum can exhibit a drop in hardness for the same reason cited for the hardness minimum location. A natural age or T6 type artificial age produces insufficient coarsening to cause a significant change in hardness. A T7 type artificial age may cause a hardness drop that corresponds to the hardness difference between the pre- and post-weld tempers (Ref 3, 18). Maximum temperatures in the HAZ during welding typically range from about 350 C at the hardness minimum to a few degrees above the temperature used for the final step of the aging of the parent material.

Experimental measurement of precipitate structure in a friction stir weld is a time-consuming and expensive process that often requires advanced, specialized apparatus. Existing thermal and microstructural models that can predict thermal profiles, microstructure, and mechanical properties from FSW processing parameters have the ability to reduce the time and expense required to optimize a FSW process (Ref 10, 14-16, 26-28). The thermal model of Khandkar et al. was calibrated using data from 7050-T74. The microstructural models of Kamp, Sullivan, and Robson were calibrated using data from 7449 and 7150 alloys. Both models have been shown to predict proper trends and supply predictions that are reasonably close to experimental measurements.

In the study described in this paper, experimental measurement of the precipitate structure across the width of a 7050-T74 friction stir weld has been made using a variety of commonly available techniques (differential scanning calorimetry (DSC), electrical conductivity, and transmission electron microscopy (TEM)). The results have been correlated with microhardness profiles. Predictions of temperatures profiles, microstructure, and hardness from models calibrated with data from 7XXX aluminum alloys are compared with the experimental precipitate structure and microhardness results with the goal of tying together disparate modeling and experimental techniques for the optimization of friction stir welding processes.

2. Materials and Methods

The material used for this study was 6.35 mm thick aluminum alloy 7050-T7451 sheet. The nominal composition of 7050 is Al-6.2Zn-2.3Cu-2.3Mg-0.12Zr (wt.%). Hardness of the parent plate was 160 HV. Electrical conductivity was 41% IACS. Friction stir welding of the characterized weld was performed at the University of South Carolina as part of a larger study investigating the effects of weld parameters on hardness profiles and temperature history (Ref 8). The specific weld parameters used were a tool rotation speed of 360 RPM, a tool translation speed of 2.54 mm/s, with a downward force of 31.1 kN. Measurement of the torque supplied to the spindle motor allowed calculation of the weld power of 1968 watts and the specific weld energy of 775 J/mm. A threaded, cylindrical tool with a dished shoulder was used. The shoulder diameter was 20.3 mm, with pin diameter and length of 7.1 and 6.1 mm, respectively, as shown in Fig. 1(a). After welding a post-weld heat treatment of 4 h at 120 C was performed to stabilize the mechanical properties and microstructure. A portion of the weld was re-stabilized 12 years later for 24 h at 120 C to evaluate whether any further changes in microhardness or microstructure would result. The purpose of the re-stabilization after such a significant time frame was to determine whether the initial post-weld heat treatment had fully stabilized the precipitate structure.
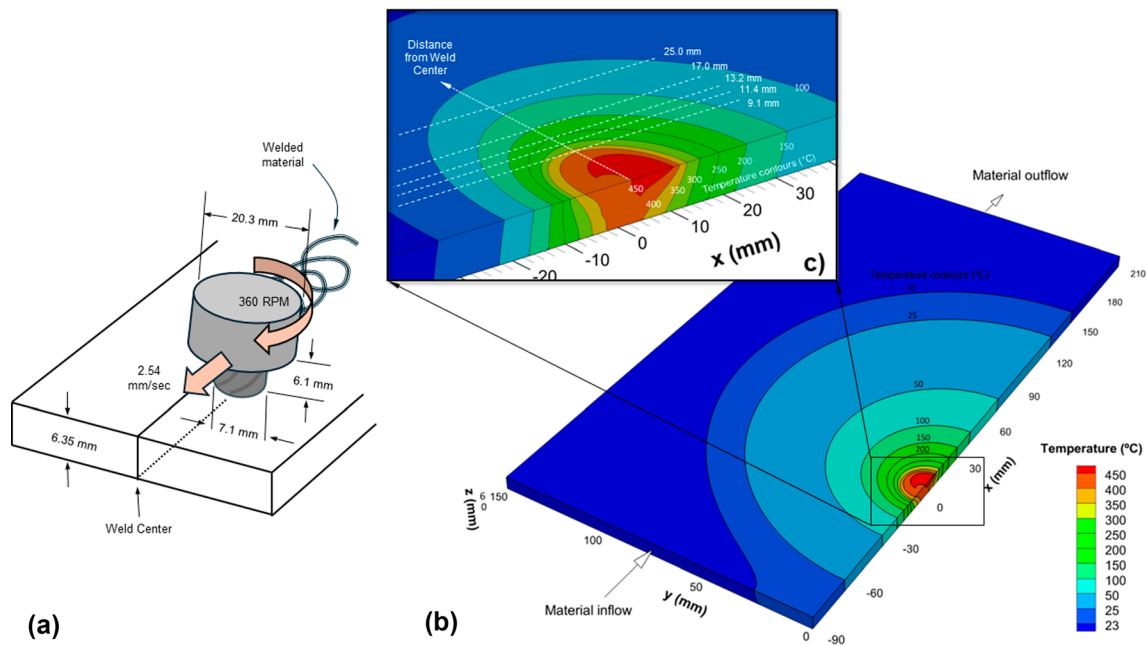
Fig. 1 (a) Experimental FSW setup showing tool and material plates. (b) Simulation domain of FSW thermal model along with maximum temperature predictions as function of position. (c) A magnified view near the tool center is shown in the inset

Microhardness measurements were made at weld mid-thickness at a spacing of 0.5 mm on both retreating and advancing sides of the weld center from the weld center into the parent material on both sides. The heat affected zone (HAZ) extended about 20 mm to either side of the weld center. Thus, microhardness measurements were made out to 25 mm on both sides. The Vickers hardness scale with an applied load of 500 g was used.

Electrical conductivity measurements were used as a qualitative measure of the change in precipitate structure as a function of location across the weld. The measurements were made with a Hocking AutoSigma 3000 electrical conductivity meter with a probe diameter of 9.5 mm. Due to the probe diameter being greater than the weld thickness, conductivity was measured on the top and bottom surfaces. After these measurements, 2.54 mm of material was machined from the bottom of the weld and a third set of measurements was made near the weld mid-thickness. Scans were made by moving the probe at 2 mm intervals from 0 to 26 mm from weld center on advancing and retreating sides. Each measurement represents the moving geometric average of a 9.5 mm circle centered at each location.

2.1 Differential Scanning Calorimetry (DSC)

DSC was used to characterize the precipitate structure as a function of position across the weld. Four cylinders, 4 mm in diameter and approximately 60 mm in length were machined from the weld mid-thickness normal to the weld plane. The cylinders spanned the entire width of the weld, were centered on the weld line, and the weld line center was marked on each cylinder. One cylinder underwent an aging treatment for 24 h at 120 C to determine the effects of a longer aging time on precipitate microstructure. A second cylinder was used for TEM specimens.

Individual DSC specimens were cut from cylinders using a Buehler low-speed diamond saw with a blade thickness of 0.45 mm. Each specimen was approximately 1.2 mm thick, with specimen centers spaced at approximately 1.7 mm along the weld width. This resulted in 25 DSC specimens (5 in the nugget, 6 in the TMAZ, 2 in the parent material, and 12 in the HAZ).

All DSC analysis was performed on a TA Instruments DSC 2910 Differential Scanning Calorimeter Q100 system. The discs with masses between 35 and 45 mg were ultrasonically cleaned for 10 min each in acetone, methanol, and isopropanol before testing. A purge gas flow rate of 50 mL/min of N_2 was used. Specimens were first equilibrated at -30 C and then heated to either 380 or 450 C at a ramp rate of 10 C/min.

2.2 Transmission Electron Microscopy (TEM)

Specimen blanks for TEM were removed at critical locations of interest to estimate the precipitate size and volume fraction as well as to identify the precipitate types present (η' and/or η). TEM specimens were removed from 0.7 to 1.0 mm thick discs, 4 mm in diameter, using focused ion beam (FIB) milling in an FEI Helios Nanolab 600i FIB using standard lift-out procedures. Final specimen dimensions were about 16 μm $\times$ 8 μm. Dark-field TEM was performed using a Phillips CM200 TEM operating at 200 kV and an FEI Talos F200X operating at 200 kV. Selected area diffraction patterns were taken along $< 100 >$, $< 110 >$, and/or $< 111 >$ directions so that diffraction from {220} planes would be present in the patterns.

2.3 Thermal Modeling

A FORTRAN three-dimensional (3-D) heat transfer model was formulated and numerically solved following a 3-D finite volume discretization method, where the governing heat transfer equation formulation was in the frame of reference of the stir weld tool (Ref 29). This simplification is significant as the transient term is eliminated from the governing heat transfer equation and the problem has been reduced to a steady state

simulation with a 3-D diffusion term and a one dimensional (1-D) convection term for material flow in the tool travel direction (x direction) as shown in Eq 1 and Fig. 1(b) and (c). In Eq 1 the term on left-hand side of the equals sign describes the convective material inflow where u is the convective inflow velocity, ρ is the density, C_p is the specific heat, and $\frac{\partial T}{\partial x}$ is the temperature gradient in the tool travel direction. The right hand side contains two types of terms: the 3-D heat diffusion terms (i.e., $k\left(\frac{\partial^2 T}{\partial x^2} + \frac{\partial^2 T}{\partial y^2} + \frac{\partial^2 T}{\partial z^2}\right)$) and the source term $S(x, y, z)$ to model the spatially variable heating due to the tool power input. Here k is thermal conductivity and x, y, and z are the spatial variables. Temperature T is a function of x, y, and z locations and in this moving reference frame the entire equation is no longer a function of time. In the computational domain shown in the figure the tool is stationary at $x = y = 0$ mm, but there is convective material inflow and outflow as shown by the arrows at a velocity of u, which is the experimental tool translation speed.

$$\rho C_p \left[u \frac{\partial T}{\partial x} \right] = k \left(\frac{\partial^2 T}{\partial x^2} + \frac{\partial^2 T}{\partial y^2} + \frac{\partial^2 T}{\partial z^2} \right) + S(x, y, z) \qquad \text{(Eq 1)}$$

Although this formulation is not capable of modeling the transient startup of the stir welding process, it has other advantages. Specifically, as compared to transient models in the laboratory reference frame the computational domain can be significantly reduced, particularly in the weld direction, thus leading to reduced cell counts and/or increased computational convergence speed or spatial resolution. Limited work was found with this same approach (Ref 30); hence, our approach here is still novel and contemporary. A power law approximation was used for the convective term and the temperature field corresponding to the solution of Eq 1 was obtained with an adaptive successive over-relaxation (SOR) numerical scheme where multiple sweeps were done throughout the domain until convergence was established in the temperature field. The following constant material properties were used in this work: the density ρ was 2830 kg/m^3, the specific heat C_p was 860 J/(kg·C) and the thermal conductivity k was 157 W/(m·C).

The computational domain was a rectangular slab corresponding to one of the aluminum alloy sheets: 6.35 mm thick, 300 mm long and 152 mm wide as shown in Fig. 1. Rectangular cells were used with a uniform mesh size throughout the domain. Symmetry was assumed in the y direction at the weld centerline surface ($y = 0$ mm), thus halving the required cell count and further improving computational efficiency. No thermal difference between the advancing and retreating sides of the tool can be captured due to this simplification. Edge face boundary surface conditions utilized convective heat losses where the convection coefficient was specified. The top boundary surface condition included both convective and radiative heat losses, although the bottom surface ($z = 0$), which would be adjacent to the backing plate during welding, included only convective losses to approximate the heat transfer. The backing plate was not modeled here, and a convective coefficient on the $z = 0$ surface was used to approximate its presence. This convective approach has shown reasonable success in the past and was deemed sufficient for the modeling fidelity of this work (Ref 26).

The model ignores any local material convection imparted by the spinning tool, and therefore does not include the effects of the convective mixing, plasticity, or surface velocity slip of the metal adjacent to the tool. The overall tool power input of 1968 W from the experimental data was modeled as a distributed power source over the surface of the tool. The total power was split into surface values for the tool tip, the vertical cylindrical surface, and the tool shoulder similar to other works (Ref 8, 30, 31). A surface heat flux boundary condition was used within the 20.3 mm diameter tool shoulder area on the top surface of the computational domain; whereas, a volumetric local cell heat generation $S(x, y, z)$ was used to model the 7.1 mm diameter circular tool tip, and the 6.1 mm long cylindrical tool pin—the latter two surfaces being both internal to the computational domain. Particular care was used to distribute the tool power values in the computational cells modeling the tool surface so that the intersected cells had surface heat fluxes or internal cell heat generation values proportional to the tool surface area that intersected each individual cell. This was done using a Monte Carlo arc-length and fractional volume computation routine.

Although various combinations of numerical model parameters were investigated, only a particular case is presented here. Specifically, the results below were modeled with 36.48 million cells, although a mesh independence study showed that even with significantly reduced cell counts as low as 4.58 million cells the temperature distribution was within approximately 0.5 °C over the entire domain. The cell size used here was $\Delta x = \Delta y = 0.25$ mm for the length and width directions, and $\Delta z = 0.127$ mm for the depth direction. Surface emissivity for the metal was chosen as 0.14 with a laboratory background temperature of 22 °C. The convective coefficients were set as 15 W/(m^2·C) for the external upstream, downstream, top and sides of the domain and 1700 W/(m^2·C) for the bottom of the plate. The bottom of the domain directly underneath the tool shoulder (22 mm diameter centered at $x = y = 0$ mm) had a 3400 W/m^2, i.e., an augmentation factor of two, to help model the increased heat transfer due to the reduced thermal contact resistance attributed to the vertical tool load. The $x = 0$ centerline side face had a convective coefficient of 0 W/m^2, to enforce an adiabatic symmetry numerical condition. The convective coefficients were chosen based on existing values in the literature and are consistent with other published FSW thermal models. For instance, Khandkar et al. (Ref 26) used the same 15 W/(m^2·K) value for the top and sides, while varying the bottom convective coefficient from 500 to 2000 W/(m^2·C) to fit their experimental data. Since no experimental temperature data were available in this work, the bottom convective coefficient and augmentation factor was varied to tune the temperature distribution to the observed maximum temperatures deduced from the microstructure and HAZ. No addition was made in the model to account for thermal losses upwards via conduction into the tool.

3. Results

3.1 Thermal Modeling

Figure 1 also shows a 3-D view of the computed results with contours plotted at temperatures of 23, 25, 50, 100, 150, 200, 250, 300, 350, 400, and 450 °C. A figure inset shows the predicted temperatures near the welding tool. The hottest region surrounds the tool which is centered at $x = y = 0$ mm, although
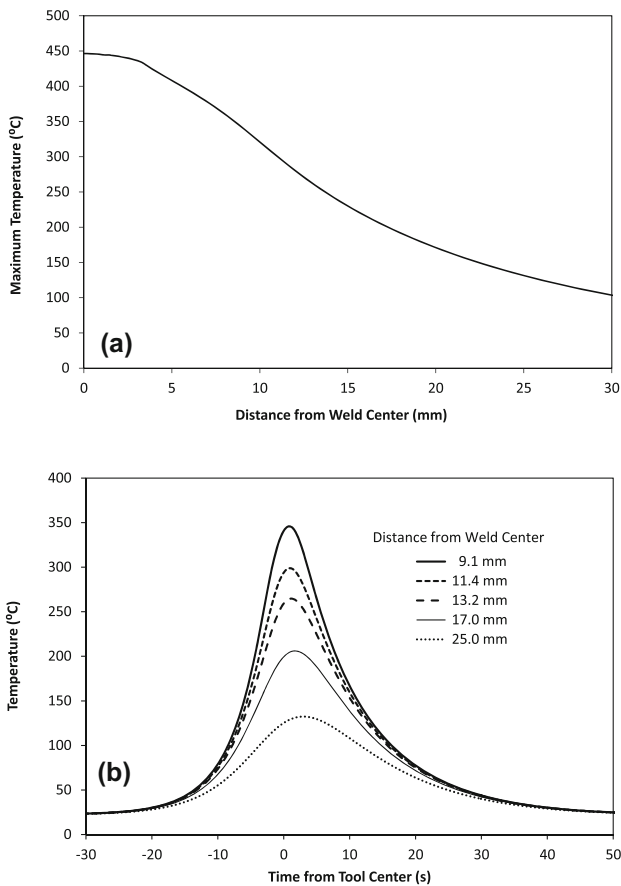
Fig. 2 (a) Maximum predicted temperature as a function of distance from weld center line. (b) Sample thermal histories at five locations in the heat affected zone

peak temperatures are downstream behind the tool center. Top surface temperatures are slightly higher than those of the bottom surface, due to the difference in convective coefficient between the two surfaces and due to the tool shoulder that acts as a heat input at the top surface.

The maximum temperature as a function of distance (y) from the weld centerline is shown in Fig. 2(a). The temperature in the figure has been computed at the vertical midplane of the aluminum alloy sheet (i.e., $z = 3.175$ mm). Due to the limitation of the thermal model, temperatures very near to the tool center and under the shoulder ($y < 10$ mm) where material mixing and plastic deformation would be present are thought to be less accurate predictions than those farther away.

Several midplane ($z = 3.175$ mm) temperature histories are shown in Fig. 2(b) for various lateral distances (y) from the weld centerline. The distances chosen in the figure correspond to the locations of the TEM samples. The time axis is referenced to the tool center ($x = 0$) and negative time represents material upstream of the tool; whereas, positive time represent downstream material which has been already welded. Locations which are closer to the weld centerline experience higher peak temperatures and longer heating durations. The peak temperatures all occur downstream of the tool center, and the peak shifts further aft as distance from the weld centerline is increased from 9.1 to 25 mm.

3.2 Microhardness

Microhardness scans measured across the entire weld at two different locations along the as-received weld length and one location along the re-stabilized weld length are shown in Fig. 3. Markers in the figure indicate boundaries between the nugget, TMAZ, HAZ, and parent material regions. Boundaries between the nugget and TMAZ as well as that between TMAZ and HAZ were determined via optical microscopy. The nugget/TMAZ boundary was located at the point where the grain structure transformed from 100% recrystallized to partially recrystallized. The TMAZ/HAZ boundary occurred at the point at which the grain orientation parallel to the plate surface to non-parallel. The parent material/HAZ boundary was defined as the point where the microhardness began to decrease from the parent material value of 160 HV.

Several notable observations can be made from Fig. 3

(i) The hardness profile exhibits a W-profile typical of that observed in T6 and T7 temper aluminum product friction stir welds.
(ii) Hardness minima are located in the HAZ approximately 9 mm from the weld center.
(iii) There are inflection points at 15 mm from the weld center in the HAZ, at which the change in hardness decrease becomes greater when approaching the weld center.
(iv) The hardness on the retreating side is 5-10 HV less than on the advancing side between the hardness minima.
(v) The hardness maximum occurs within 0.5 mm of the nugget/TMAZ boundary.
(vi) The hardness for the re-stabilized weld is slightly greater than the as-received weld. The difference is greatest in the nugget and in the vicinity of the hardness minimum.
(vii) The nugget, TMAZ and HAZ extend out to 3.5, 5.5, and 20 mm from the weld center, respectively.

3.3 Electrical Conductivity

Electrical conductivity at weld mid-thickness is plotted in Fig. 4. Conductivity ranges from 32% IACS at the center to 41% IACS at distances 14 mm and greater from the weld center. These two values of conductivity are consistent with T6 and T74 tempers, respectively, in 7050. The rapid change in conductivity between 2 and 10 mm indicates that changes in solute content of the solid solution, precipitate size and precipitate volume fraction are changing most rapidly in this region.

3.4 DSC

DSC scans for age-hardened aluminum alloys provide temperatures at which precipitate formation (exothermic) and dissolution (endothermic) reactions occur. The specific reaction that takes place at each peak must be identified using other means, typically TEM. A search of the literature over the past 40 years correlating peak temperature with precipitate reactions in 7XXX aluminum alloys shows consistent agreement at the temperatures at which each step in the precipitation sequence occur. (Ref 19, 25, 32-41) Thus, the precipitate reaction
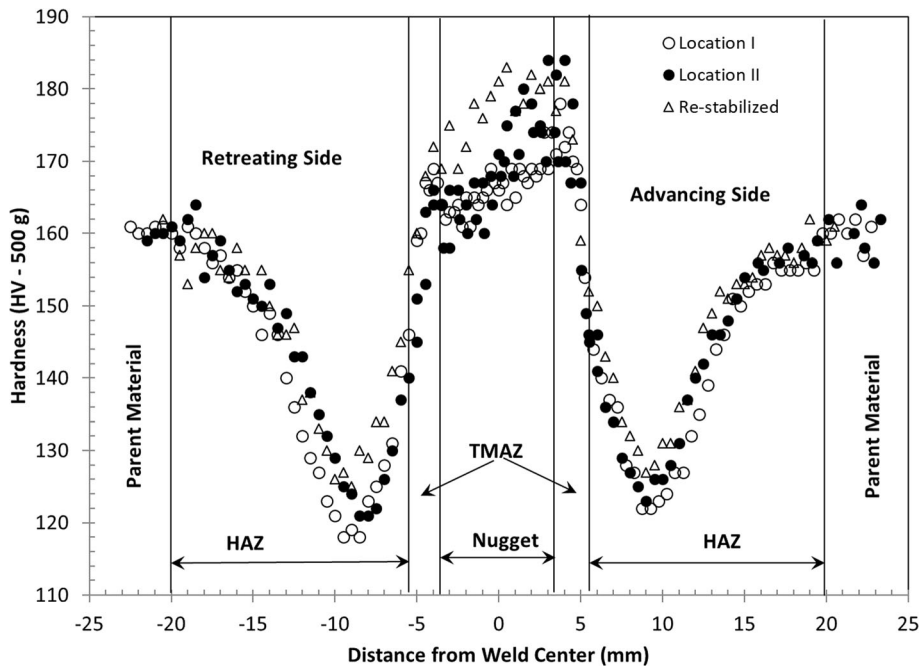
Fig. 3 Microhardness scan across friction stir weld at two locations along as-received weld and one location along re-stabilized weld
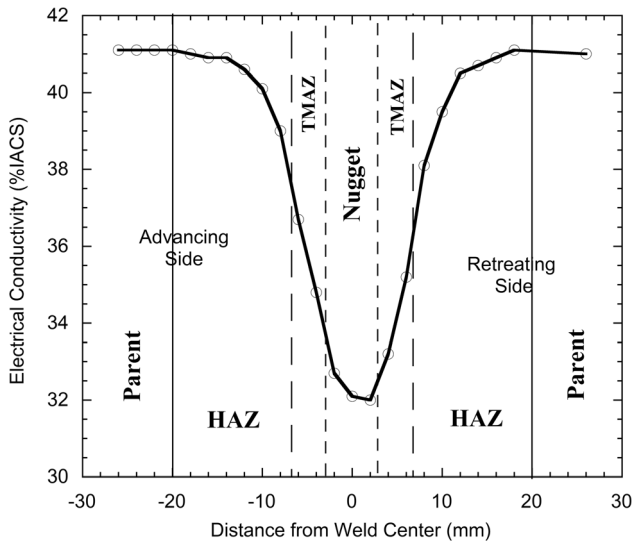

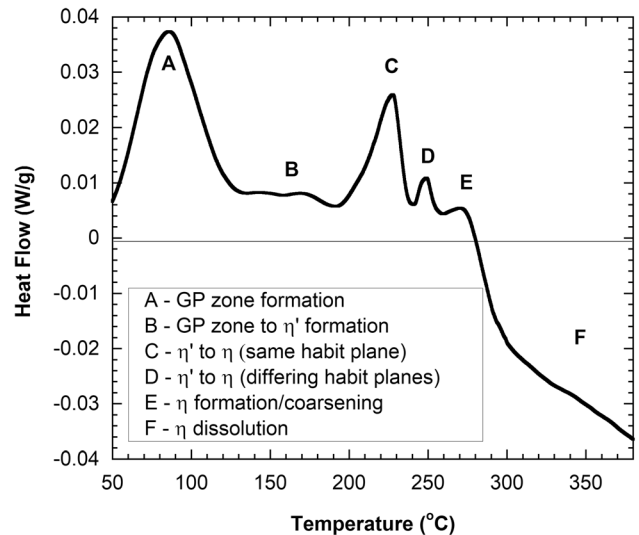Fig. 4 Electrical conductivity across friction stir weld

Fig. 5 DSC Scan of as-quenched 7050 illustrating exothermic precipitate formation peaks

associated with each peak was identified via the literature in the current work, rather than TEM analysis.

DSC scans were generated to document the change in precipitate structure as a function of position within the weld. Potential precipitate formation, exothermic, peaks for 7050 are shown in Fig. 5. The scan used parent material that was solutionized at 475 C and held in a freezer at − 15 C until immediately prior to the DSC scan. Effects A through F are denoted in the figure along with descriptions of the most widely accepted precipitate reactions associated with each effect. The ordering of effects A through F is consistent with the precipitation sequence

$$SSS \rightarrow GPzones \rightarrow metastable\ \eta' \rightarrow stable\ \eta.$$
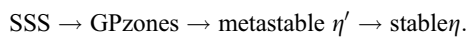
DSC scans from specimens on the advancing side of the weld, covering the range of locations from the nugget to the parent material, are shown in Fig. 6(a) through (d). The four scans in Fig. 6(a) depict behavior in the outer HAZ, at 17-25 mm from weld center, in which the microhardness decreases at a slow rate as the weld center is approached.

Precipitate behavior in 7XXX alloys between 200 and 290 C is complex with multiple reactions (η' dissolution, η formation/coarsening, and η dissolution) occurring simultaneously. Peak II in Fig. 6(a) corresponds to the region in which η' dissolution is the dominant reaction. The temperature at which this peak begins depends on the size of the η' precipitates, which in turn is a function of the previous thermal treatment. This peak begins at about 165 C, which corresponds to the
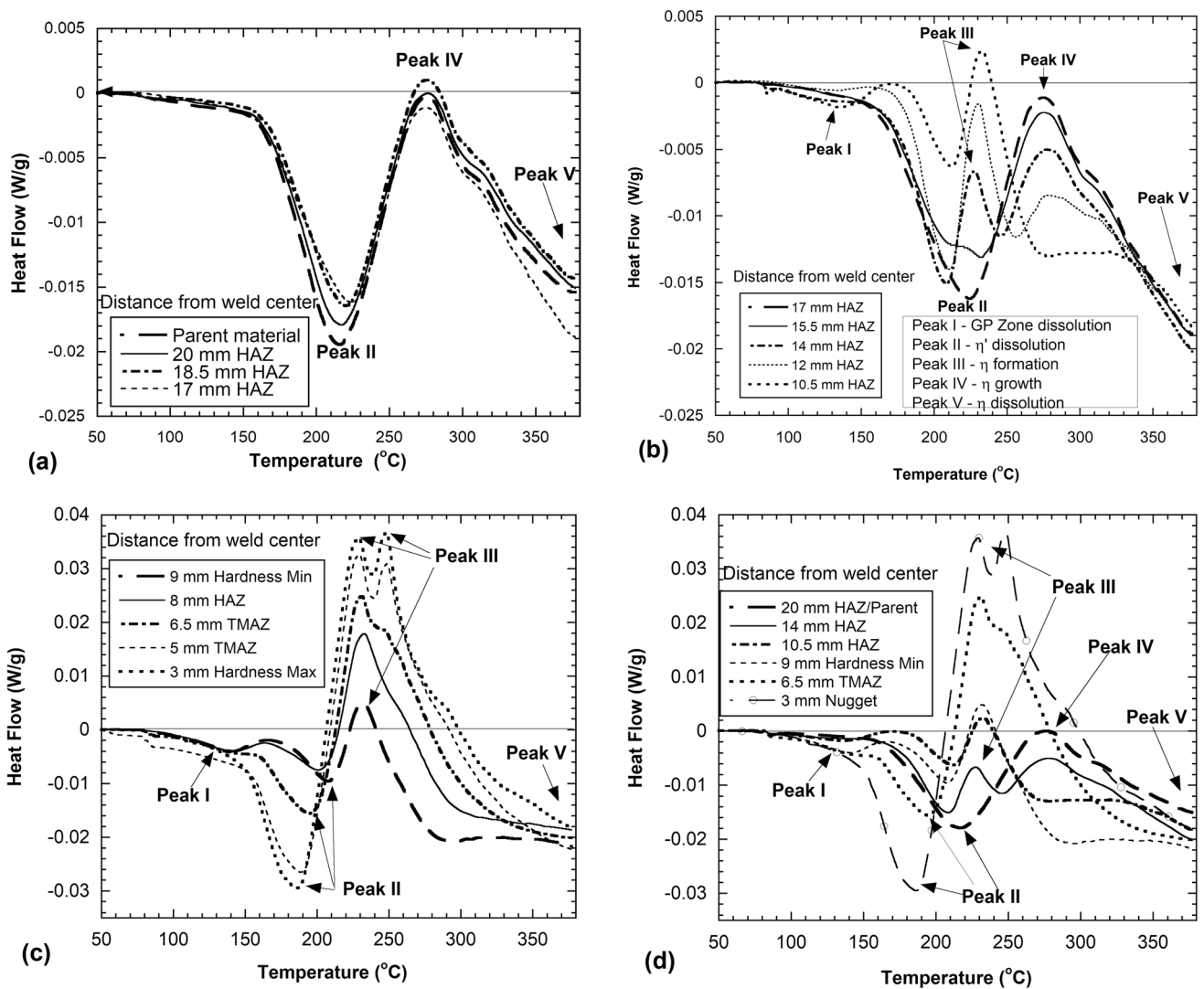
Fig. 6 DSC Scans at different locations along the width of a 7050-T74 friction stir weld (a) outer HAZ (b) inner HAZ (c) hardness minimum to nugget (d) sample locations across entire weld

temperature typically used in the second step of a commercial T74 aging process. Thus the smallest η' precipitates should begin to dissolve at this temperature. Maximum heat flow values for peak II occur at about 220 C. Peaks IV and V represent the competing effects of formation/coarsening and dissolution of η precipitates. Formation/coarsening dominates at temperatures below approximately 290 C. The result is an exothermic peak due to formation/coarsening of larger η precipitates over top of an endothermic peak due to dissolution of smaller η' and η precipitates. Dissolution dominates at temperatures above 292 C.

Figure 6(a) shows the DSC scans for locations 25-17 mm from the weld center. The maximum temperatures experienced during welding in this region range from about 170 C, at 25 mm, to 205 C, at 17 mm, in which a portion of the smaller η' precipitates are expected to dissolve and the larger η' precipitates to transform and coarsen slightly to η phase. The area beneath peak II decreases by about 20%, indicating a similar decrease in the precipitate volume fraction. (a 20% decrease in precipitate volume fraction corresponds roughly to a decrease in Vickers hardness of 8 for 7050. This agrees reasonably well with the results in Fig. 3). The small decrease in area of peak IV

indicates less coarsening of η phase, indicating a small increase in coarse η precipitates in this region of the weld.

DSC scans for locations 17-10.5 mm from weld center are shown in Fig. 6(b). This corresponds to the HAZ region in Fig. 3 where the rate of hardness decreases more rapidly up to the hardness minimum. The maximum temperatures experienced in this region of the HAZ, from Fig. 2(a), range from about 205 C at 17 mm to about 320 C at 10.5 mm. Several observations can be made as the weld center is approached.

(i) Areas beneath peaks II and IV continue to decrease until peak IV is no longer present at 10.5 mm. The decrease in area beneath peak II is associated with increased dissolution of η' precipitates with increasing temperature during welding. Peak IV is associated with formation and coarsening of η phase precipitates. The decrease in area beneath peak IV is due to transformation and coarsening of η' to η phase during the weld cycle.

(ii) An exothermic peak III first appears at 15.5 mm on top of the endothermic peak II. Peak III is centered at 230 C and corresponds to η' transformation to η during the DSC scan. The η' precipitates that transform during the

DSC scan formed during the initial post-weld heat treatment. The area under this peak increases as the location in the weld approaches the center.

(iii) At 12 mm the η' dissolution peak onset increases by 10-175 C. The onset increases further to 185 C at 10.5 mm. This observation indicates that the peak temperature during welding at a location between 12 and 14 mm exceeded 250 C, resulting in significant precipitate coarsening.

(iv) A small endothermic peak I, centered at about 135 C appears at 10.5 mm. In 7XXX series alloys an endothermic peak at this temperature is typically associated with GP zone dissolution. The GP zones formed during the 12 years period between the initial post-weld heat treatment and the DSC scan as a result of a small supersaturation of the matrix during welding.

These observations are consistent with an increase in temperature during welding from that which causes only partial precipitate dissolution at 17 mm, to a range in which both dissolution and coarsening occur at 10.5 mm.

DSC scans covering the area between the hardness minimum and nugget are shown in Fig. 6(c). The maximum temperatures experienced in this region are estimated, in Fig. 2(a), to range from about 350 C at 9 mm (the hardness minimum) to about 430 C in the nugget. A number of trends in this region can be noted

(i) The area under peak III continues to increase as the weld center is approached. Peak III separates into a doublet in the TMAZ and nugget with the size of the higher temperature peak in the doublet increasing as the weld center is approached. The presence of peak III is a result of GP zones and η' precipitates that form during the post-weld heat treatment and transform to η precipitates during the DSC scan.

(ii) Both the onset and peak heat flow temperatures of peak II decrease to 150 C and 185 C, respectively, with closer proximity to the weld center. This is likely due to sufficient solute supersaturation in this region after welding. A fine distribution of η' precipitates was produced during the post-weld aging treatment that resulted in reduced peak II DSC scan temperatures.

(iii) The area under peak II increases as the volume fraction of η' precipitate formed during the post-weld aging treatment increases.

(iv) The area under peak I at the hardness minimum increases from that at 10.5 mm and remains constant from the hardness minimum to the nugget.

3.5 Restabilized Specimen DSC

Figure 7(a) and (b) show DSC scans for weld material that was re-stabilized for 24 h at 120 C. The re-stabilization occurred 12 years after welding with material at room temperature. The scans in Fig 7(a) are for the nugget and parent material. The re-stabilization treatment has little to no effect on the parent material. Peak II in the re-stabilized nugget material starts at a temperature about 40 C greater and peaks about 10 C greater than for the post-weld aged material. This may indicate that either a small quantity of GP zones formed during the 12 years natural aging period and transformed to η' precipitates

during re-stabilization or that the smallest η' precipitates formed during the initial post-weld aging coarsened during re-stabilization. The Peak III doublet in the re-stabilized material is slightly smaller than for the post-weld stabilized material.

The DSC scan in Fig. 7(b) shows the response at a distance between 10.5 and 10.9 mm from the weld center. This behavior is typical of that observed between 6 and 18 mm from the weld center. The magnitude of the changes increases from a minimum at 6 mm, peaking at between 10 and 11 mm, and then decreasing as the distance from weld center increases to 18 mm. The changes are most significant between 8 and 13 mm from weld center and maximum between 10 and 11 mm. In this range, the re-stabilization heat treatment results in the replacement of endothermic Peak I with a small exothermic η' formation peak at 140 C, an increase in both the starting temperature and the area under Peak II, little to no change in the area under Peak III, and an increase in the area under Peak IV. These changes all point toward formation of GP zones during the 12 years of natural aging due to a small matrix supersaturation still present after the post-weld heat treatment. The re-stabilization treatment caused transformation of these GP zones to small η' precipitates and the coarsening of the η' present after the initial post-weld heat treatment. Specifically, the formation of η' precipitates is inferred from the elimination of Peak I and area increase under Peak II. The coarsening is indicated by the Peak II starting temperature increase and area increase under Peak IV.

3.6 TEM

Sample dark-field TEM photographs of η precipitates at locations 13.2 and 9.1 mm from the weld center are shown in Fig. 8(a) and (b). Qualitatively, it is apparent that the average precipitate diameter is larger and the precipitate volume fraction is lesser at 9.1 mm than at 13.2 mm from the weld center. The calculated peak temperatures at these locations from Fig. 2 are 260 and 350 C, respectively. Microstructural modeling calculations in Kamp et al. indicate that the average precipitate size at 9.1 mm should be about twice that at 13.2 and the volume fraction significantly greater at 13.2 mm (Ref 26). The photographs qualitatively support these predictions.

4. Discussion

Friction stir welding imposes a short, non-isothermal temperature excursion on the material in and near the weld. Using typical welding parameters, the excursion lasts from 45 s to 2 min with the time spent above 200 C lasting 15-40 s (Ref 8). For aluminum alloys of the thickness and welding parameters used in this study, the maximum temperature attained is more important in predicting the changes in precipitate microstructure during welding than the time spent at temperature. The initial response of precipitates to a sudden temperature increase is dissolution of small precipitates whose diameter is less than a critical size. This may be followed by coarsening of the surviving precipitates and/or transformation to a more stable precipitate form, such as transformation of η' to η precipitates. In typical overaged 7XXX aluminum alloys the η' precipitates begin to dissolve at about 170 C (Ref 22). The dissolution rate accelerates above 190 C. Precipitate coarsening and transformation from η' to η begins around 220-230 C.
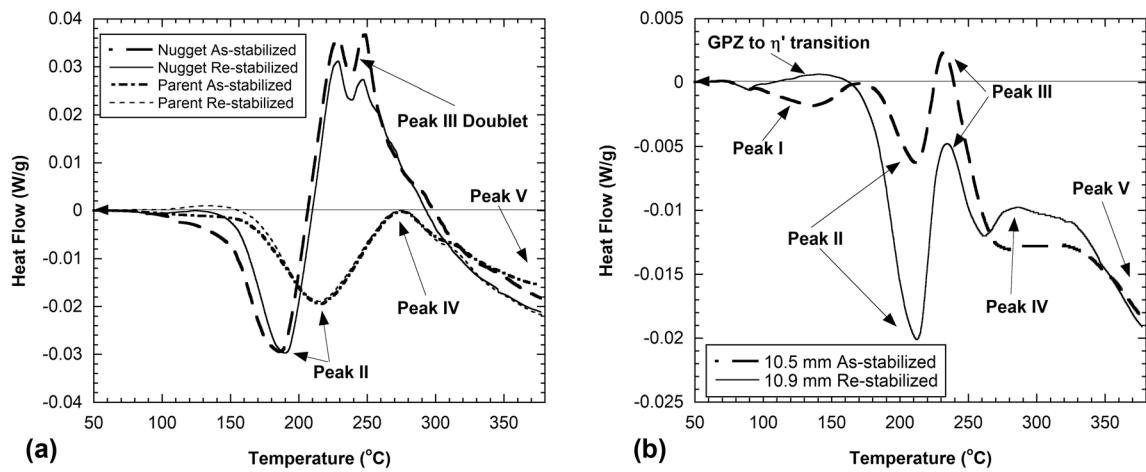
Fig. 7 Comparison of DSC scans from post-weld stabilized and re-stabilized material from 7050-T74 friction stir weld (a) nugget region and parent material (b) HAZ near hardness minimum
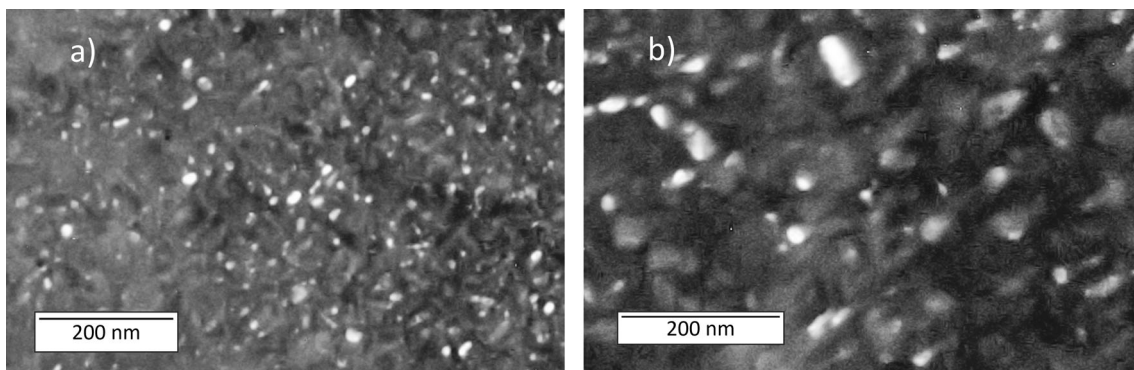

Fig. 8 Dark-field TEM photographs of η precipitates at: (a) 13.2 mm and (b) 9.1 mm from weld center

Above 225 C, a sufficient amount of precipitates have dissolved to create enough supersaturation for the material to respond to a T6-type post-weld heat treatment (aged at 121 C for 24 h) to increase strength (Ref 8, 6). Significant amounts of η precipitates begin to dissolve around 320-330 C accompanied by a significant increase in matrix solute that results in precipitation after welding. All precipitates will have dissolved by the time the temperature reaches about 430 C (Ref 16, 28).

The temperature profiles generated in Fig. 2 agree well with those presented by Reynolds et al. (Ref 10) and Kamp et al. (Ref 16), who used the same welding parameters as used in the current study. The following discussion uses the temperature profiles in Fig. 2, the microhardness and conductivity results in Fig. 3 and 4, and the results from the DSC scans in Fig. 6 and 7 to compare with microstructural predictions discussed above.

The outer HAZ region from 17 mm to the parent material experienced maximum temperatures between 170 and 205 C. Microstructure models predict that some precipitate dissolution should occur with little to no coarsening. There is no change in electrical conductivity and a 5% drop in microhardness in this range. The DSC scans in Fig. 6(a) indicate a small drop in precipitate content with no significant change in the η growth/coarsening peak.

The HAZ region from 17 to 14 mm experienced temperatures from 205 to 245 C. Microstructure models predict that precipitate dissolution should accelerate, precipitate coarsening should begin, and sufficient matrix supersaturation should

occur such that a post-weld aging treatment should produce a small amount of fine η' precipitates. The electrical conductivity and microhardness begin to decrease more rapidly in this region, which is consistent with increasing dissolution. The DSC scans in Fig. 6(b) provide more fidelity. The scan at 15.5 mm shows the first evidence of fine η' precipitates produced by post-weld aging (a small Peak III superimposed over Peak II). The maximum temperature at this point was 220 C, which corresponds to the point where precipitate coarsening and η' to η transformation should begin. The DSC scan at 14 mm shows the first evidence of significant coarsening of η precipitates. The decrease in area beneath Peak IV (growth / coarsening of η) is associated with precipitate coarsening during overaging of 7XXX aluminum alloys (Ref 34). The maximum temperature at this point was 245 C, which corresponds to the point where η precipitates begin to coarsen rapidly. (Ref 8, 28)

The peak temperatures in the central portion of the HAZ region from 14 to 9 mm range from 245 to 340 C. All the η' precipitates dissolve or transform to η at the low end of this temperature range. As temperature increases, the large η precipitates continue to coarsen, resulting in a microstructure of large, widely spaced precipitates immediately after welding (Ref 28). This results in an overaged, low strength, high electrical conductivity state with an increasingly supersaturated matrix as temperature increases. Precipitation during cooling and a T6-type post-weld aging would produce a distribution of

fine η' precipitates, which would increase hardness and decrease electrical conductivity. Figure 4 shows that the electrical conductivity decreases in this range, primarily due to the η' precipitates formed during the post-weld age. Microhardness decreases primarily due to wide spacing between η precipitates. There are two features in the DSC scans of Fig. 6(b) and (c) that confirm the presence of larger η precipitates. The first being the increase in the onset temperature of Peak II (dissolution of η precipitates) from 150 to 170 C. The second being the decreasing area beneath Peak IV (formation/growth of η precipitates) as peak temperature in the weld increases. The increased precipitate dissolution during welding and increased production of η' during the post-weld age is confirmed due to the increasing area beneath Peak III (transformation of η' to η) with increasing peak welding temperature. Hardness minima in FSW 7050-T7 are generally found to be in the region in which the peak maximum temperature is between 320 and 350 C, which is consistent with these results (Ref 8).

The peak temperatures in the inner HAZ, TMAZ, and nugget range from about 340 to 435 C. This corresponds to distances from weld center ranging from 9 to 0 mm. During welding, the large η precipitates begin to dissolve at the low end of this temperature range and are completely or almost completely dissolved at the high end. Some η' precipitates form during the cooling portion of the weld cycle. Additional η' precipitates form during the post-weld aging (Ref 16, 28, 42). The replacement of coarse, widely spaced η precipitates with fine, closely spaced η' precipitates produces an increase in hardness and a decrease in electrical conductivity as shown in Fig. 3 and 4. A number of significant changes are noted in the DSC scans as the location approaches the weld center in this range. First, there is a small GP zone dissolution peak centered at 140 C. These GP zones were likely formed via natural aging during the 12 years period between welding and performing the DSC scan. Second, the onset temperature of Peak II decreases from 170 to 150 C between 9 and 5 mm and then ceases to decrease further. This observation indicates that the coarse η precipitates formed during welding were largely dissolved at 5 mm, where the peak temperature calculated in Fig. 2(a) is about 410 C. This is reasonably close to the published η solvus in 7050 of 425 C. Third, the area beneath the endothermic Peak II (η' dissolution) increases as the weld center is approached. The rate of increase becomes greater as the peak weld temperature exceeds 360-385 C, which occurs at locations of 8 mm and 6.5 mm from the weld center. This observation is consistent with increasing dissolution of coarse η precipitates resulting in increased matrix supersaturation as temperatures during welding increase. The increased supersaturation results in increased weight percentage of fine η' precipitates during the post-weld age. The increases in area beneath Peaks III and IV in Fig. 6(c) are due to the transformation of η' to η during the DSC scan and are not necessarily indicative of any changes in the post-weld microstructure.

4.1 Restabilized Specimens DSC Scans

As shown in Fig. 7, the DSC scans of the specimens re-stabilized at 120 C for 24 h after 12 years of natural aging show small changes compared to the as-stabilized material, particularly in the region between 8 and 13 mm from the weld center, where the maximum peak temperatures ranged from 360 C at 8 mm to 250 C at 13 mm. In Fig. 7(b), there is a

comparison of DSC scans at 10.5-10.9 mm from the weld center for the as-stabilized and re-stabilized specimens. There is a noticeable GP zone dissolution peak (Peak I) in the as-stabilized scan that is absent from the re-stabilized scan. The area beneath Peak II in the re-stabilized scan has increased to the size observed in the TMAZ of the as-stabilized material of Fig. 6(c). The presence of these peaks show that GP zones formed during the long period of natural aging following the post-weld stabilization and then transformed to η' precipitates during the re-stabilization treatment. This occurs predominately in the weld region between 8 and 13 mm, where the peak temperatures were between 360 and 250 C), and in which precipitation dissolution was small. In this region, the matrix supersaturation due to dissolution was insufficient to produce η' precipitates when utilizing a T6 type post-weld aging treatment at 120 C. This temperature range is significant as that between the point where substantial η precipitate coarsening begins and the temperature where coarse η precipitates are most stable prior to dissolution. DSC scans in Fig. 6(b) and (c) for this region generally show small endothermic GP zone dissolution peaks of about -0.002 W/g and small η' dissolution peaks less than -0.01 W/g in height. Small increases in microhardness on the order of 4-5 MPa are observed in Fig. 3 for the re-stabilized material in this region.

The metastable solvi temperatures for GP zones and η' precipitates decrease with decreasing cooling rate and matrix supersaturation. This is due to low vacancy content and supersaturation. The aging treatment used for post-weld stabilization utilizes a temperature that is below the GP zone and η' solvi for quickly quenched material and fully supersaturated matrices of standard high-strength 7XXX aluminum alloys. This allows the formation of GP zones and η' precipitates during aging. However, this temperature is likely above the GP zone and η' solvi at low supersaturation levels and slow cooling rates. This results in no precipitation of these metastable phases during aging. The decrease in solvi temperatures and low vacancy content may be overcome by utilizing a 2-step age where the first step temperature is reduced. The 2nd step is reached by utilizing a ramp rate that is slow enough that the GP zones generated in the first step do not dissolve during heat-up to the 2nd step temperature. It is possible that the use of such a post-weld aging treatment could be utilized to avoid the decrease in strength often observed near the hardness minimum during a post-weld heat treatment. A first step aging temperature between 75 and 95 C, followed by a slow ramp to a second step at 120 C may provide a more adequate post-weld aging than one designed for a fully saturated, quickly quenched material.

The data generated in this study has been used in conjunction with microstructure evolution predictions of other authors to determine whether the use of multiple, closely spaced DSC scans, microhardness, and thermal modeling can be used to validate the evolution models and be used for design of friction stir welding processes. For the material and processes used in this study, it was noted that the microhardness inflection point at 14 mm from weld center corresponds to a peak temperature of 250 C and the beginning of significant η precipitate coarsening. The hardness minimum at 9 mm from weld center corresponds to a peak temperature of 345 C and the beginning of significant η precipitate dissolution. The transition from the TMAZ to the nugget at 3.5 mm from weld center corresponds to a peak temperature near the η phase solvus and the dissolution of all or most of the η precipitates. This work

shows that careful analysis of DSC peaks combined with thermal analysis, microhardness, electrical conductivity and TEM correlates well with microstructural models found in the literature.

5. Conclusions

A combination of thermal modeling to predict temperature profiles and peak temperatures as a function of location, closely spaced differential scanning calorimetry, microhardness, electrical conductivity, and TEM was successfully used to qualitatively and semiquantitatively characterize the precipitate structure and hardness as a function of position through a 7050 aluminum alloy friction stir weld.

Precipitate evolution in the outer HAZ of the weld (located 14-20 mm from weld center, and peak temperature < 250 C), consisted of precipitate dissolution, transformation from η' to η, slight coarsening, and a small decrease in hardness.

Transformation from η' to η was completed, coarsening was accelerated, and precipitate dissolution continued in the mid-HAZ region to the hardness minimum (located 9-14 mm from weld center, and 250 C < peak temperature < 340 C). This was accompanied by a steeper decrease in hardness.

From the hardness minimum to the nugget (located less than 9 mm from weld center, and 340 C < peak temperature < 410 C) coarse η precipitates increasingly dissolved with rising peak temperatures, resulting in more matrix supersaturation. Subsequent post-weld aging produced an increased volume fraction of η' precipitates and an increase in hardness.

The inflection point in the hardness curve from a slight to steep decrease in hardness corresponded to exceeding a peak temperature of 250 C and accelerating rate of precipitation coarsening.

The hardness minimum in the hardness curve occurred where the peak temperature was approximately 340 C, precipitate coarsening and spacing was near maximum, and matrix supersaturation after welding was low.

Natural aging occurred after welding and stabilization over a 12 year period in the region from 8 to 13 mm from the weld center. This corresponded to peak welding temperatures of 260-360 C) where the matrix supersaturation immediately after welding was insufficient to result in η' precipitation when aging at 120 C. The natural aging produced a small increase in hardness over time. A two-step post-weld stabilization procedure consisting of aging at 75-95 C followed by a slow ramp to 120 C is proposed to eliminate the observed decrease in hardness near the hardness minimum during post-weld aging.

The data generated was compared to microstructural predictions of non-isothermal temperature excursion precipitate evolution models from the literature. The microstructures and hardness trends indicated by data generated in this study agreed well with the microstructure and strength predictions of the models.

Acknowledgments

Conflict of interest

The authors declare that they have no conflict of interest.

References

1. E. Cross, D.L. Olson, and S. Liu, *Handbook of Aluminum Physical Metallurgy and Processes*, Marcel Dekker, New York, 2003, p 481–532

2. M. Dumont, A. Steuwer, A. Deschamps, M. Peel, and P.J. Withers, Microstructure Mapping in Friction Stir Welds of 7449 Aluminum Alloys Using SAXS, *Acta Mater.*, 2006, **54**, p 4793–4801

3. M. Nicolas and A. Deschamps, Precipitate Microstructures and Resulting Properties of Al-Zn-Mg Metal Inert Gas-Weld Heat-Affected Zones, *Metall. Mater. Trans. A*, 2004, **35A**, p 1437–1448

4. J.Q. Su, T.W. Nelson, R. Mishra, and M. Mahoney, Microstructural Investigation of Friction Stir Welded 7050–T651 Aluminum, *Acta Mater.*, 2003, **51**, p 713–729

5. K.V. Jata, K.K. Sankaran, and J.J. Ruschau, Friction-Stir Welding Effects on Microstructure and Fatigue of Aluminum Alloy 7050–T7451, *Metall. Mater. Trans. A*, 2000, **31A**, p 2181–2192

6. M. Nicolas and A. Deschamps, Characterisation and Modelling of Precipitate Evolution in an Al-Zn-Mg Alloy During Non-Isothermal Heat Treatments, *Acta Mater.*, 2003, **51**, p 6077–6094

7. W.H. Mahoney, C.G. Rhodes, J.G. Flintoff, R.A. Spurling, and W.H. Bingel, Properties of Friction-Stir-Welded 7075 T651 Aluminum, *Metall. Mater. Trans. A*, 1998, **29A**, p 1955–1964

8. A.P. Reynolds, W. Tang, Z. Khandkar, J.A. Khan, and K. Linder, Relationships Between Weld Parameters, Hardness Distribution and Temperature History in Alloy 7050 Friction Stir Welds, *Sci. Technol. Weld. Joining*, 2005, **10**, p 190–199

9. J. Yan and A.P. Reynolds, Effect of Initial Base Metal Temper on Mechanical Properties in AA7050 Friction Stir Welds, *Sci. Technol. Weld. Joining*, 2009, **14**, p 582–587

10. P. Upadhyay and A.P. Reynolds, Effects of Thermal Boundary Conditions in Friction Stir Welded AA7050-T7 Sheets, *Mater. Sci. Eng. A*, 2010, **527**, p 1537–1543

11. F. De Geuser, B. Malard, and A. Deschamps, Microstructure Mapping of a Friction Stir Welded 2050 Al-Li-Cu in the T8 State, *Philos. Mag.*, 2014, **94**, p 1451–1462

12. A. Steuwer, M. Dumont, J. Altenkirch, S. Birosca, A. Deschamps, P.B. Prangnell, and P.J. Withers, A Combined Approach to Microstructure Mapping of an Al-Li AA2199 Friction Stir Weld, *Acta Mater.*, 2011, **59**, p 3002–3011

13. S. Harpreet and R.S. Mishra, Aging kinetics of Friction Stir Welded Al-Cu-Li-Mg-Ag and Al-Cu-Li-Mg Alloys, *Mater. Des.*, 2016, **110**, p 60–71

14. J.D. Robson, N. Kamp, and A. Sullivan, Microstructural Modeling for Friction Stir Welding of Aluminum Alloys, *Mater. Manuf. Processes*, 2007, **22**, p 450–456

15. A. Sullivan and J.D. Robson, Microstructural Properties of Friction Stir Welded and Post-Weld Heat-Treated 7449 Aluminium Alloy Thick Plate, *Mater. Sci. Eng. A*, 2008, **A478**, p 351–360

16. N. Kamp, A.P. Reynolds, and J.D. Robson, Modelling of 7050 Aluminum Friction Stir Welding, *Sci. Technol. Weld. Joining*, 2009, **14**, p 589–596

17. P.L. Threadgill, A.J. Leonard, H.R. Shercliff, and P.J. Withers, Friction Stir Welding of Aluminum Alloys, *Int. Mat. Rev.*, 2009, **54**, p 49–93

18. R.W. Bush, M. Kiyota, and C. Kiyota, Characterization of a Friction Stir Weld in Aluminum Alloy 7055 Using Microhardness, Electrical Conductivity, and Differential Scanning Calorimetry (DSC), *Metall. Mater. Trans. A*, 2016, **47**, p 3522–3532

19. C.B. Fuller, M.W. Mahoney, M. Calabrese, and L. Micona, Evolution of Microstructure and Mechanical Properties in Naturally Aged 7050 and 7075 Al Friction Stir Welds, *Mater. Sci. Eng. A*, 2010, **527**, p 2233–2240

20. A. Pastor and H.G. Svoboda, Time-Evolution of Heat Affected Zone (HAZ) of Friction Stir Welds of AA7075-T651, *J. Mater. Phys. Chem.*, 2013, **1**, p 58–64

21. I. Kalemba, C. Hamilton, and S. Dymek, Natural Aging in Friction Stir Welded 7136–T76 Aluminum Alloy, *Mater. Des.*, 2014, **60**, p 295–301

22. F. Viana, A.M.P. Pinto, H.M.C. Santos, and A.B. Lopes, Retrogression and Re-Aging of 7075 Aluminum Alloy: Microstructural Characterization, *J. Mater. Process. Technol.*, 1999, **92–93**, p 54–59

23. T. Marlaud, A. Deschamps, F. Bley, W. Lefebvre, and B. Baroux, Evolution of Precipitate Microstructures during the Retrogression and Re-Aging Heat Treatment of an Al-Zn-Mg-Cu Alloy, *Acta Mater.*, 2010, **58**, p 4814–4826

24. J.M. Papazian, Differential Scanning Calorimetry Evaluation of Retrogressed and Re-aged Microstructures in Aluminum Alloy 7075, *Mat. Sci. Eng.*, 1986, **79**, p 97–104

25. J.K. Park and A.J. Ardell, Correlation Between Microstructural Behavior of Aluminum Alloy 7075 and Al-Zn-Mg Alloys in Various Tempers, *Mat. Sci. Eng.*, 1989, **A114**, p 197–203

26. M.Z.H. Khandkar, J.A. Khan, and A.P. Reynolds, Prediction of Temperature Distribution and Thermal History During Friction Stir Welding: Input Torque Based Model, *Sci. Technol. Weld. Joining*, 2003, **8**, p 165–174

27. N. Kamp, A. Sullivan, R. Tomasi, and J.D. Robson, Modelling of Heterogeneous Precipitate Distribution Evolution During Friction Stir Welding Process, *Acta Mater.*, 2006, **54**, p 2003–2014

28. N. Kamp, A. Sullivan, and J.D. Robson, Modelling of Friction Stir Welding of 7xxx Aluminum Alloys, *Mat. Sci. Eng. A*, 2007, **466**, p 246–255

29. S.V. Patankar, *Numerical Heat Transfer and Fluid Flow*, CRC Press, Boca raton, 1980

30. M. Song and R. Kovacevic, Thermal Modeling of Friction Stir Welding in a Moving Coordinate System and Its Validation, *Int. J. Mach. Tools Manuf.*, 2003, **43**, p 605–615

31. D.M. Neto and P. Neto, Numerical Modeling of the Friction Stir Welding Process: A Literature Review, *Int. J. Adv. Manuf. Tech.*, 2013, **65**, p 115–126

32. J. Buha, R.N. Lumley, and A.G. Croskey, Secondary Ageing in an Aluminum Alloy 7050, *Mat. Sci. Eng. A*, 2008, **492**, p 1–10

34 A. Yamamoto, K. Minami, U. Ishihara, and H. Tsubakino, Calorimetric and Resistivity Study of Formation and Redissolution of Precipitates in 7050 Aluminum Alloy, *Mat. Trans. JIM*, 1998, **39**(1), p 69–74

34. X.M. Li and M.J. Starink, DSC Study on Phase Transitions and Their Correlation with Properties of Overaged Al-Zn-Mg-Cu Alloys, *J. Mater. Eng. Perform.*, 2012, **21**(6), p 977–984

35. R. Delasi and P. Adler, Calorimetric Studies of 7000 Series Aluminum Alloys – 1. Matrix Precipitate Characterization of 7075, *Met. Trans. A*, 1977, **8A**(7), p 1177–1183

36. J.M. Papazian, Calorimetric Studies of Precipitation and Dissolution Kinetics in Aluminum Alloys 2219 and 7075, *Met. Trans. A*, 1982, **13A**, p 761–769

37. M.J. Starink and X.M. Li, A Model for the Electrical Conductivity of Peak aGed and Overaged Al-Zn-Mg-Cu Alloys, *Metall. Mater. Trans. A*, 2003, **34A**, p 899–911

38. X.J. Wu, A.K. Koul, and L. Zhao, A New Approach to Heat Damage Evaluation for 7xxx Aluminum Alloy, *Can. Aeronaut. Space J.*, 1996, **42**, p 93–101

39. S. Gupta, R.S. Haridas, P. Agrawal, R.S. Mishra, and K.J. Doherty, Influence of Welding Parameters on Mechanical, Microstructure and Corrosion Behavior of Friction Stir Welded Al 7017 Alloy, *Mat. Sci. Eng. A*, 2022, **846**, p 143303

40. N. Martinez, N. Kumar, R.S. Mishra, and K.J. Doherty, Microstructural Comparison of Friction-Stir-Welded Aluminum Alloy 7449 Starting from Different Tempers, *J. Mater. Sci.*, 2018, **53**, p 9273–9286

41. L. Luo, B. Yang, X. Yang, W. Yan, C. Gan, X. Liu, and J. Wang, Effects of Different Cooling Conditions on Microstructure and Precipitation Behavior of Fine-Grained Al-Zn-Cu-Mg Alloy Friction Stir Welding Joint, *J. Mater. Res. Technol.*, 2023, **24**, p 4534–4550

42. P. Chen, T. Li, X. Lin, Y. Tang, G. Liu, S. Wang, B. Huang, and Z. Zhang, The Precipitate Evolution in Friction Stir Welding of 2195-O Al-Li Alloy, *J. Mater. Res. Technol.*, 2023, **24**, p 1991–2006